

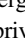
Thermodynamic Limits of Sperm Swimming Precision

C. Maggi ^{*}, F. Saglimbeni, V. Carmona Sosa, and R. Di Leonardo

*Soft and Living Matter Laboratory, NANOTEC-CNR, Institute of Nanotechnology, 00185 Rome, Italy
and Dipartimento di Fisica, Sapienza Università di Roma, Piazzale Aldo Moro 2, 00185 Rome, Italy*

B. Nath

*Dipartimento di Fisica, Sapienza Università di Roma, Piazzale Aldo Moro 2, 00185 Rome, Italy;
ISC-CNR, Institute for Complex Systems, Piazzale Aldo Moro 2, 00185 Rome, Italy;
and Mechanical Engineering Department, National Institute of Technology Silchar, 788010 Assam, India*

A. Puglisi 

*Dipartimento di Fisica, Sapienza Università di Roma, Piazzale Aldo Moro 2, 00185, Rome, Italy
and ISC-CNR, Institute for Complex Systems, Piazzale Aldo Moro 2, 00185 Rome, Italy*



(Received 21 March 2023; accepted 20 June 2023; published 20 July 2023)

Sperm swimming is crucial to fertilize the egg, in nature and in assisted reproductive technologies. Modeling the sperm dynamics involves elasticity, hydrodynamics, internal active forces, and out-of-equilibrium noise. Here we give experimental evidence in favor of the relevance of energy dissipation for sperm beating fluctuations. For each motile cell, we reconstruct the time evolution of the two main tail's spatial modes, which together trace a noisy limit cycle characterized by a maximum level of precision p_{\max} . Our results indicate $p_{\max} \sim 10^2 \text{ s}^{-1}$, remarkably close to the estimated precision of a dynein molecular motor actuating the flagellum, which is bounded by its energy dissipation rate according to the thermodynamic uncertainty relation. Further experiments under oxygen deprivation show that p_{\max} decays with energy consumption, as it occurs for a single molecular motor. Both observations are explained by conjecturing a high level of coordination among the conformational changes of dynein motors. This conjecture is supported by a theoretical model for the beating of an ideal flagellum actuated by a collection of motors, including a motor-motor nearest-neighbor coupling of strength K : When K is small the precision of a large flagellum is much higher than the single motor one. On the contrary, when K is large the two become comparable. Based upon our strong-motor-coupling conjecture, old and new data coming from different kinds of flagella can be collapsed together on a simple master curve.

DOI: [10.1103/PRXLife.1.013003](https://doi.org/10.1103/PRXLife.1.013003)

I. SWIMMING WITH NOISE

Sperm motility plays a crucial role in sexual reproduction and also serves as a prototype for understanding the physics of microswimmers [1,2]. Its investigation is fundamental to develop new technologies, for instance, to improve fertility diagnostics and assisted reproduction techniques [3]. It can also positively influence the fields of artificial microswimmers and microfluidic devices [4].

A sperm cell is composed of a large head (spatulate shaped for bull sperms such as those considered here) and a thin whiplike tail called a flagellum, whose oscillatory movement sustains a traveling wave from head to tail [5]. In recent decades, physics has investigated the sperm swimming problem, how it originates from flagellar beating coupled with

the fluid dynamics and with the many possible boundary conditions [6–8]. Different swimming modes have been identified, including planar beating near flat (e.g., air-liquid or liquid-substrate) surfaces, beating with precession when the head is anchored to a point, circular trajectories on a plane, three-dimensional helical in the bulk, etc. [9].

In modeling, minimal ingredients for swimming of semi-flexible filaments are an anisotropic Stokes drag and a single traveling wave, e.g., for small deviations $y(t, s)$ from the straight rod shape at time t and arclength $s \sim x$, $y(t, x) = A \cos(kx - \omega t)$, which guarantees irreversibility of the shape cycle, i.e., $y(t, x) \neq y(T - t, x)$, where T is the cycle period, necessary to swim at low Reynolds numbers [10,11]. An important element is noise, that is, deviations from the average flagellum beating dynamics, which has been previously considered in modeling [7,12–14] and in experiments, with *Chlamydomonas* [15–19] and with sperms [20]. In particular, such experimental works have estimated through different methods the quality factor of the phase noise in the beating cycle, a parameter which is strictly connected to the precision studied here, as discussed later. Flagellar fluctuations have been observed to influence self-propulsion [21] and synchronization of adjacent filaments [16,17,22].

^{*}claudio.maggi@roma1.infn.it

Published by the American Physical Society under the terms of the [Creative Commons Attribution 4.0 International](https://creativecommons.org/licenses/by/4.0/) license. Further distribution of this work must maintain attribution to the author(s) and the published article's title, journal citation, and DOI.

In the present study we show how energy dissipation, an intrinsic quantity for motors at all scales, affects noise in sperm beating, rationalizing the problem under the framework of thermodynamic uncertainty relations (TURs) [23–25] (see Appendix D for a summary of the simplest working principle behind TURs). Remarkably, the connection between power consumption and macroscopic fluctuations leads us to put forward a hypothesis about the collective dynamics of the molecular motors actuating the flagellum.

The sperm axoneme hosts an array of dynein molecules for a total of $N \sim 10^5$ motor domains [26–28]. Each motor converts available ATP molecules into power strokes inducing local bending of the axoneme. Deviations from the average biochemical cycle of a molecular motor occur mainly because of fluctuating times of residence in the different chemical states [29]. Less understood is the mechanism of coordination of the N motors necessary to generate the tail’s traveling wave: A widely accepted fact is the presence of some feedback mechanism inducing activation and deactivation of the motors based upon the local bending state [30]. The hypothesis that a dynein operates independently of its neighbors is questioned by the observation (in micrographs by scanning electron

microscopy, etc.) of nonrandom grouping of dynein states and by the evidence that interactions between adjacent dyneins may be inevitable because of the size of dynein arms [31–33]. Our experimental observations about the high amplitude of the noise affecting flagellum beating (comparable to that of a dynein motor) and about the decay of flagellum precision with energy consumption (similar to what happens for a single motor) contribute together to conjecture a strong coupling between the dynamics of adjacent motors proteins. A schematic model for axonemal oscillations under the effect of noisy motor dynamics corroborates our hypothesis.

II. PRECISION OF A BROWNIAN MOTOR

We first discuss how to measure precision, an observable which has recently attracted a profound interest in nonequilibrium statistical physics (see Fig. 1). For our purpose it is sufficient to consider a system where an angular observable $\theta(t)$ represents the system’s configuration [see Figs. 1(a) and 1(b)]. We expect $\theta(t)$ to perform an irreversible stochastic stationary dynamics with average drift $\langle \theta(t) - \theta(0) \rangle = Jt$ and relative dispersion $\langle [\theta(t) - \theta(0) - Jt]^2 \rangle \sim 2Dt$ for large t .

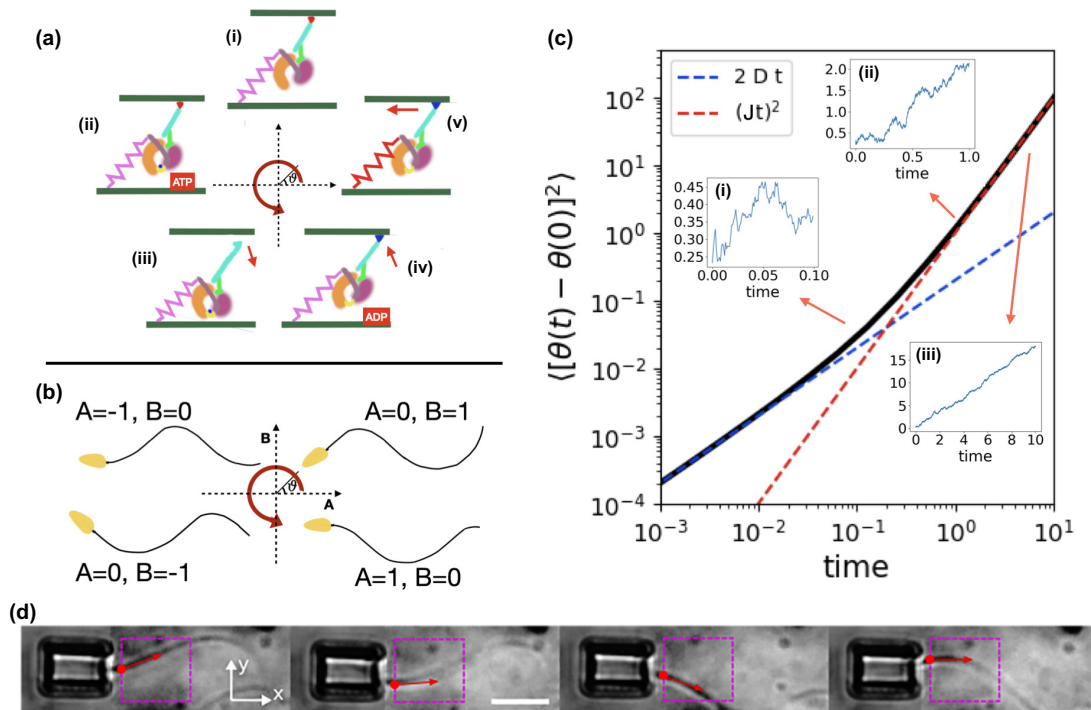


FIG. 1. Precision of stochastic clocks. Examples are shown, in different systems, of the coarse-grained coordinate $\theta(t)$ useful to define the precision p of Brownian clocks. (a) Sketch of the supposed chemical cycle of the dynein ATP-ase, counterclockwise starting from the top: (i) rest (apo) state, (ii) ATP-binding, (iii) detachment of the stalk, (iv) $\text{ATP} \rightarrow \text{ADP} + \text{P}$ reaction with rejoining of the stalk to the upper substrate, in a forward position, and (v) stroke of the linker (red spring) with consequent dragging of the upper substrate. (b) Sketch of the elastomechanical cycle of a sperm cell. The tail shape is approximated by a curve close to $A(t)\cos(kx) + B(t)\sin(kx)$. (c) Mean-square displacement from a trajectory generated by the numerical integration of the equation $\dot{\theta} = J + \sqrt{2D}\eta(t)$, with $\eta(t)$ white noise with unitary amplitude, $J = 1$, and $D = 0.1$. The insets show the trajectory $\theta(t)$ with a different time range, i.e., (i) $t \in [0, 0.1]$, (ii) $t \in [0, 1]$, and (iii) $t \in [0, 10]$. It is evident how the mean current $\bar{\theta} = J$ can be appreciated only at times much larger than $1/p = D/J^2$. (d) Successive snapshots [taken at 0.04-s intervals with an optical microscope (see Appendix A)] of the tail dynamical sequence in a caged sperm experiment. The purple box represents the region of interest and the red dot and red arrow identify the parameters a and b (y position and slope of the tail close to the origin, respectively) which approximate A and B in Eq. (3), here corresponding to $(A, B) \sim (0, 1) \rightarrow (-1, 0) \rightarrow (0, -1) \rightarrow (1, 0)$. The white arrows indicate the \hat{x} and \hat{y} directions (the \hat{z} direction is perpendicular to both). The white scale bar represents 10 μm .

We are interested in the precision rate defined as

$$p = \frac{J^2}{D}. \quad (1)$$

The observable p can be understood as the inverse of the typical time $t^* = 1/p$ separating the diffusive regime $t \ll t^*$ [$Dt \gg (Jt)^2$] from the ballistic regime $t \gg t^*$ [see Fig. 1(c) and its insets].

The quantity p has been demonstrated, through the so-called thermodynamic uncertainty relation [23–25], to be bounded from above by the entropy production rate or in practical terms (for the purpose of steady isothermal molecular motors) the motor’s energy consumption rate \dot{W} in thermal units:

$$p \leq p_{\text{TUR}} = \frac{\dot{W}}{k_B T}. \quad (2)$$

The ratio $\mathcal{Q} = p/p_{\text{TUR}} \leq 1$ can be considered as a motor’s figure of merit. Estimates of p through Markovian models informed by experimental data [34] suggest that several molecular motors work not far from their optimum, or at least close to its order of magnitude ($\mathcal{Q} \geq 0.1$). In the following we present a method to estimate p and we apply it to experiments with bulls’ sperm cells [see Figs. 1(b) and 1(d)]. Notwithstanding its physical relevance, the quantity p has not been discussed for microswimmers, even if its estimate can be deduced from other variables in previous works. Quantities that are strictly related to p are the dissipation time [35] and the quality factor $q = J/2D = p/2J$, which has been measured within a similar approach for *Chlamydomonas* flagella in [15–19] and for bull sperms in [20], although never compared to energy dissipation or discussed within the framework of TURs.

III. PRECISION OF SPERM BEATING

We adopt a coarse-graining protocol that reduces the space of possible shapes of the flagellum into two coordinates, the minimum for the existence of irreversible limit cycles. We improve the quality of image tracking and disentangle the simplest mode of sperm movement, that is, the planar one, with the following technique. Each observed sperm has its head trapped in a microcage printed by two-photon microolithography [see Fig. 1(d) and Appendix A]. The cell cannot spin and the flagellum beats on the $\hat{x}\hat{y}$ plane. While the most common swimming strategy of sperm cells is helical [9,36], planar movement is typically observed close to a surface and can lead to circular paths [37–39], here prevented by the cage. The sperm’s center of mass has a very limited dynamics in the $\hat{x}\hat{z}$ plane but can oscillate in the transverse \hat{y} direction; the body, entirely free, performs planar tail beating, which pushes the body into the cage, making the escape probability negligible. As a direct consequence of tail beating, the head is also observed to oscillate: Our main results are obtained by tail tracking, while in the Supplemental Material we confirm our conclusions by tracking the head (see [40] and Fig. S1 therein).

Referring to Fig. 1(d), our region of interest (ROI) tracks less than half of the observed beating wavelength. After

image processing (see Appendix B) each tail’s image is fitted through a second-order polynomial $y(x, t) = a(t) + b(t)x + c(t)x^2$ (see also the movie in the Supplemental Material [40]). Under the assumption that the ROI contains less than half a wavelength [and therefore $y(x, t)$ has at most one extremal point], $a(t)$ and $b(t)$ are (but for multiplicative constants) fair approximations of the coefficients $A(t)$ and $B(t)$, respectively, of a mode expansion

$$y(x, t) \approx A(t) \cos(kx) + B(t) \sin(kx) \\ \underset{x \rightarrow 0}{\sim} A(t) + kB(t)x + O(x^2). \quad (3)$$

Such a shape approximation and the consequent coarse graining of the planar flagellum dynamics into two main coordinates A and B have been used for bull sperms [20], with *Chlamydomonas* flagella [15–19] and with human sperms [39]. A similar approach to the breakdown of detailed balance in flagella has been adopted in experiments with *Chlamydomonas* [41], with filaments in actin-myosin networks [42], with *C. elegans* worms [43]. A general perspective about this strategy was discussed in a recent review [44]. In experiments of this kind, however, precision and TUR are rarely considered [45,46].

For the purpose of estimating p for each cell, we first apply a filter to the $a(t)$ and $b(t)$ time series in order to remove low-frequency drifts, including average, and normalize the data to have a standard deviation of 1. We observe that the two coordinates exhibit almost harmonic oscillations at a similar frequency $f \sim 6\text{--}8$ Hz [see spectra in Appendix B, Figs. 6(b) and 6(c)] but with a phase delay $\Delta(t)$ that fluctuates around a steady nonzero value [Fig. 6(a)]. This delay allows us to reconstruct the angle $\theta(t)$ in the $a(t)$ - $b(t)$ plane [see Fig. 2(a)] and finally measure the average phase-space current $J = \langle \dot{\theta}(t) \rangle / t$ [see Fig. 2(b)]. Apart from a few noise-dominated cells where J is small and negative we find $J > 0$, as expected from the geometrical interpretation of $a(t)$ and $b(t)$ in terms of the main modes of the tail’s shape. A negative J would correspond to a waveform traveling in a direction that is incompatible with forward swimming. We stress that the cumulative phase-space angle $\theta(t)$ is proportional to the number of performed cycles of the sperm’s tail shape dynamics. The average current $|J|$ is related to the beating frequency f in a subtle way: In fact, the growth of $\theta(t)$ is influenced not only by the oscillation of $a(t)$ and $b(t)$ but also by the sign of their phase delay Δ . Failures to guarantee a constant sign of Δ imply *ineffective beatings*, i.e., uncoordinated oscillations which do not contribute to the growth of $\theta(t)$, leading to $|J| \leq J_{\text{max}} = 2\pi f$.

Fluctuations of the rotation speed $\dot{\theta}(t) - J$ are clearly visible in our experiment [see Figs. 2(b) and 2(c)] and represent departures from the average shape cycle $\theta_{\text{ideal}}(t) = Jt$. They are due in part to real dynamical noise (stochastic deviations) and in part to the fact that the real shape dynamics is slightly different from the approximated one (deterministic deviations). Since deterministic deviations are periodic and each experiment includes hundreds of beating periods, their contribution to the diffusivity D can be safely neglected for our purpose. The main origin of stochastic deviations is nonequilibrium fluctuations, acting both on the

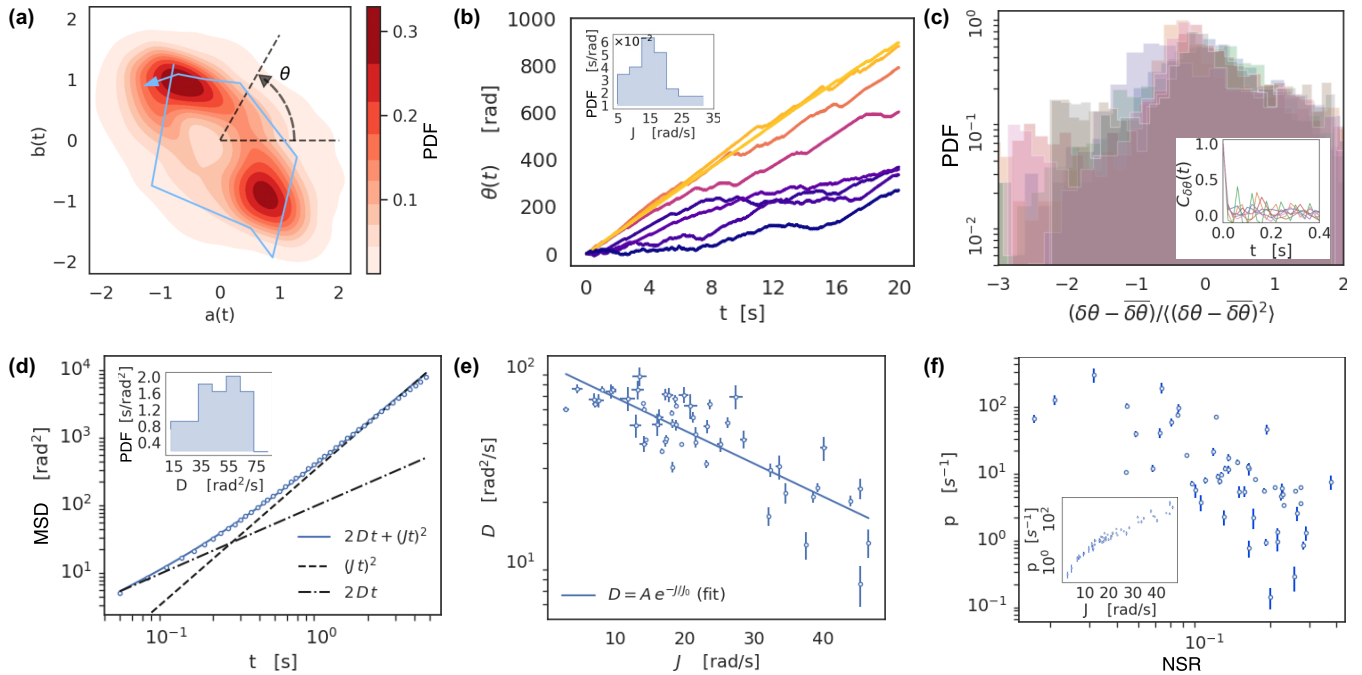


FIG. 2. Extracting precision from tail tracking. (a) Histogram of the positions in the plane $a(t)$ - $b(t)$ for the 12 sperm with precision $p > 20 \text{ s}^{-1}$. The light blue curve traces the $a(t)$ - $b(t)$ path for a particular sperm in 0.2 s (10 frames). (b) Integrated phase-space current $\theta(t)$ for a few observed sperm. The inset shows the probability density function (PDF) (over all observed sperm) of the average current J . (c) PDF (over a 20-s acquisition), for a few sperm, of $\delta\theta = \theta(t + dt) - \theta(t)$ (shifted by the mean and scaled by the standard deviation), where $dt = 0.02 \text{ s}$. The inset shows a few autocorrelations $C_{\delta\theta}(t) = \langle \delta\theta(t)\delta\theta(0) \rangle$, where $\delta\theta = \delta\theta - \langle \delta\theta \rangle$. (d) Mean-square displacement of $\theta(t)$ for a given sperm and its fit according to the model $\text{MSD}(t) = 2Dt + (Jt)^2$. The inset shows the PDF of diffusivity D over all observed sperm. (e) Diffusivity D versus average current J together with decaying exponential fit $D \sim 10^2 e^{-J/25} \text{ s}^{-1}$. (f) Precision p versus the noise-to-signal ratio (NSR) computed from the signals $a(t)$ and $b(t)$. The inset shows p versus the current J . In (e) and (f) error bars for J and D denote 3 times the standard deviation of J and D estimated when fitting the MSD by χ^2 optimization. Data come from the observation of 54 different sperm cells, if not specified otherwise.

fluid surrounding the flagellum and on the working cycle of the thousands of molecular motors actuating the flagellum. At low Reynolds numbers the first effect is negligible (see Appendix B 2).

We empirically find a good fitting model for the mean-square displacement $\langle [\theta(t + \tau) - \theta(t)]^2 \rangle \sim J\tau + 2D\tau^2$ (averaged over t along each whole experiment) [see Fig. 2(d) for an example]. Alternative ways to estimate the diffusivity are discussed in [20]; we have considered them for our experiment, finding substantial agreement (see Fig. S2 in the Supplemental Material [40]). In Fig. 2(e) we show the relation between diffusivity D and average current J displaying an average decay but with wide population variability. In Fig. 2(f) we plot the measured values of p in a large set of experiments, as a function of the noise-to-signal ratio [defined as the ratio between the peak of the spectrum and its average at frequencies higher than the oscillation frequency (see Fig. 6 in the Appendix B)] and, in the inset, versus J . Our first main conclusion is that p takes values in the approximate range $0 - p_{\max}$ with $p_{\max} \approx 10^2 \text{ s}^{-1}$. Moreover, we see that it roughly decreases with the noise-to-signal ratio and it roughly increases with J . A visual inspection of the extremal cases, i.e., those close to 0 and those close to p_{\max} , confirm that they correspond to chaotic motion and to almost regular periodic motion, respectively.

IV. SPERM PRECISION IS MUCH LOWER THAN THE TUR BOUND

Direct empirical estimates of the energy consumption (through respiration and glycolysis) for various types of sperm gave figures in the range of $(10^7 - 10^8)k_B T \text{ s}^{-1}$ (see Appendix B) [27,47,48]. Theoretical estimates for the power produced by microswimmers are given by the Taylor formula, here adapted for bull sperm [48]:

$$\dot{W}_{\text{prod}} \approx \pi^3 \eta L f^2 \beta^2. \quad (4)$$

Here β is the tail beating amplitude, L is the tail length, and η the host fluid viscosity (we have assumed, in the original Taylor formula, the cross section of the flagellum to be approximately $0.2 \mu\text{m}$ and the tail wavelength approximately $35 \mu\text{m}$). We set $\beta = 5 \mu\text{m}$ (only weakly varying with external conditions in our range; see [49]), $L = 60 \mu\text{m}$, and $\eta = 10^{-3} \text{ Pa s}$. The accepted order of magnitude of the sperm's efficiency is approximately 10–25% [50–55], giving values which are compatible with experimental estimates $\dot{W} \approx 10^8 k_B T \text{ s}^{-1}$ when $f = 20 \text{ Hz}$ at 37°C . In our experiments at room temperature, approximately 20°C , the typical beating frequency is 6–7 Hz, leading to $\dot{W} \approx 10^7 k_B T \text{ s}^{-1}$, and therefore $p_{\text{TUR}} = 10^7 \text{ s}^{-1}$. It is clear that all these figures rest in a much narrower range if the normalized consumption

rate is considered $\dot{W}/f^2 \approx (2-5) \times 10^6 k_B T$ s. In conclusion, the bound in Eq. (2) largely overestimates our measured maximum precision, with $Q_{\text{macro}} = p_{\text{max}}/p_{\text{TUR}} \sim 10^{-5}$. In the following we propose an interpretation of this result.

An intriguing observation concerns the maximum precision, computed from empirical data-informed models, of the dynein molecular motors p_d [34], which is close to the maximum values we have measured for the whole flagellum $p_d \sim p_{\text{max}}$ [56]. Our interpretation of the similarity between those two figures is the following. Let us denote by $\theta_i(t)$ the integrated current, in the space of motor configurations, in the time t for the i th dynein motor. In both the systems (sperm's flagellum and dynein) the current integrated in time counts the cumulative number of performed cycles in the configuration space. We conjecture that, in a given amount of time, the number of cycles in the configuration space of the sperm's flagellum is proportional to the number of cycles in the motor configuration space of *any* molecular motor in that flagellum, i.e., $\theta(t) \approx C\theta_i(t) \forall i \in [1, N]$, with possible i -dependent corrections which rapidly vanish with t . The result of this conjecture is that the precision of the variable $\theta(t)$ is close to the precision of variables $\theta_i(t)$ for any i . The biological meaning of our conjecture is that a long-range coordination among molecular motors inside the flagellum, quite an accepted fact in the literature [30], affects also fluctuations. In order to make our conjecture more robust, we proceed along two different paths: a new theoretical model and a second experiment.

V. A MODEL WITH STRONGLY COUPLED MOTORS

A first clue in support of our conjecture comes from the numerical analysis of a theoretical model for the motor-actuated flagellar dynamics, extensively studied in Refs. [12,57,58], modified here through the introduction of a coupling term between adjacent motors. The model is depicted in Fig. 3(a) and is described in detail in Appendix C. It consists of a filament with N motors. Each motor acts on the filament through an interaction potential and performs a stochastic attachment-detachment dynamics which breaks the detailed balance as if consuming ATP. The motor position X oscillates under the joint effect of the forces of the attached motors and an external elastic force $\xi \dot{X}(t) = -\partial_X \sum_i s_i U[x_i - X(t)] - \kappa X$, with $s_i \in \{0, 1\}$ representing the detached-attached status of the i th motor, the motor-filament potential $U(x) = U_0[1 - \cos(2\pi x/\ell)]$, viscosity ξ , and elastic constant of the external spring κ . The elastic force here could represent the effect of the cage but in previous studies was introduced just to simplify the mathematics of the problem; it is not crucial for the model's phenomenology [57]. The variables s_i jump from 0 to 1 and back according to a Poisson process. In the original model the probability rates of such a process depended only upon the local motor-filament potential, so the fluctuations of the jump dynamics of each motor were independent of nearby motors; for this reason the amplitude of the macroscopic noise was observed to decrease with N [20]. Here we employ a binding potential $K(s_i - s_{i+1})^2$ that correlates the states s_i and s_{i+1} of adjacent motors. Increasing K (from the case $K = 0$, which corresponds to the original version) drastically changes the behavior of the model, in particular, resulting in a much

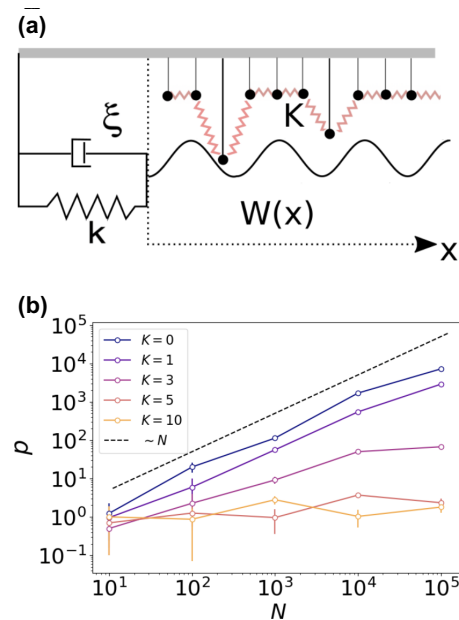


FIG. 3. Theoretical model. (a) Sketch of the model. (b) Precision p versus number of motors N for different choices of the coupling parameter K , showing the $O(N)$ scaling for uncoupled motors ($K = 0$) and the $O(1)$ scaling for large K . In all the simulations we have used $\alpha = \eta = 0.5$, $k/\xi\Omega = 10$, and $\alpha NU_0/\Omega\ell^2\xi = 0.6$. The error bars are obtained to error propagation based upon the error in the measurement of D . Such error is the estimated standard deviations of D in the nonlinear least-squares fit of the exponential decay of the phase correlation (see Appendix C).

stronger macroscopic noise, i.e., a largely faster decay of the phase correlation (see Fig. 7 in Appendix C).

In Fig. 3(b) we draw our main new conclusion, measuring the precision $p = \omega^2/D$, where ω is the average oscillation frequency and D the diffusivity deduced from the decay of phase correlation [20]. When $K = 0$ the precision grows linearly with N , in agreement with what was already observed in [20] and with the reasonable argument that the N random independent fluctuations of the motor phases contribute with a variance $1/N$ to the fluctuations of the macroscopic phase. However, the noise reduction due to the growth of N disappears at large K : When K increases the size scaling of p goes from $p \sim O(N)$ to $p \sim O(1)$. This result amounts to saying that the precision of the whole flagellum becomes comparable to the precision of the single motor when K is large enough, as in the experiment. On the other hand, the energy consumption (ATP consumed per cycle and per motor) increases with N , mostly independently of the coupling strength. The ratio between precision $p \sim O(1)$ and energy consumption $\dot{W} \sim N$ therefore decreases as $1/N$, in fair agreement with our experimental observations.

VI. EXPERIMENT UNDER OXYGEN DEPRIVATION

Experimentally, we reconsider the TUR [Eq. (2)]. For a single dynein motor, in fact, it establishes a *close* upper bound: $Q_{\text{micro}} = p_d/(\dot{W}_{\text{dynein}}/k_B T) \gtrsim 10^{-1}$. The closeness of the bound suggests that a variation of energy consumption must result in a proportional variation of dynein's precision,

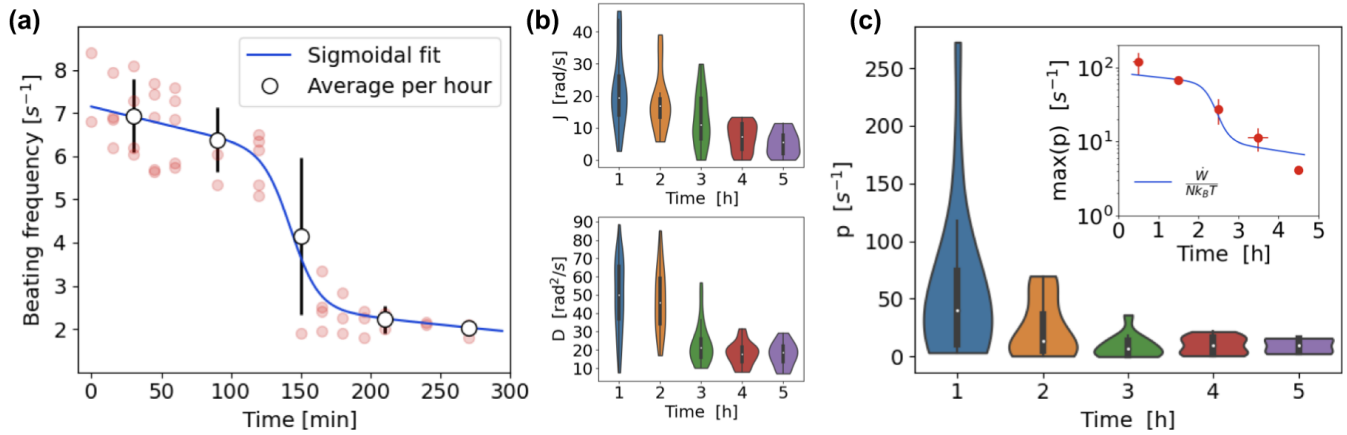


FIG. 4. Sperm precision and thermodynamics. Observations were made for caged sperms in experiments within a sealed chamber. (a) Decay of beating frequency [as measured from the spectrum peak of $a(t)$ and $b(t)$] with time. The average values of the frequencies at each hour of the experiment are also marked as white circles, together with a sigmoidlike fit $f(t) = c_1 e^{-c_2 t} s(t) + c_3 e^{-c_4 t} [1 - s(t)]$ with sigmoid $s(t) = [1 + e^{(t-t_0)/\tau}]^{-1}$ and best-fit values $t_0 = 143$, $\tau = 10.2$, $c_1 = 7.1$, $c_2 = 1.1 \times 10^{-3}$, $c_3 = 3.5$, and $c_4 = 2 \times 10^{-3}$. (b) Reduction of average current and diffusivity along time, shown as violin plots, each from an hour bin (e.g., 1 means all observation is done in the first hour, etc.). (c) Decay of precision with time, again in the form of a violin plot. The inset shows the decay of p_{\max} (estimated as the average of the top 25% population) together with the normalized (by $N = 10^5$) power consumption extracted by the Taylor formula [Eq. (4)] using the frequency decay fit shown in Fig. 3(a), with amplitude fixed at the average observed value $5.2 \mu\text{m}$. Error bars represent standard deviations normalized by the square root of the number of data in the aforementioned percentile. The sizes of samples in (b) and (c) are 41 sperms in the first hour, 24 in the second hour, 34 in the third hour, 25 in the fourth hour, and 16 in the fifth hour.

confirmed also in theoretical models [34]. Therefore, if the noise of the flagellum beating is dominated by molecular motors' noise, a reduction of energy consumption should result in a reduction of the flagellum's p_{\max} .

We have performed a series of experiments in oxygen deprivation (see Fig. 4). The samples were left in a sealed box for several hours, recording activity and assessing the p of all trapped cells, every 15–30 min. During the total time of the experiment (5 h) we observed a clear decay in the beating frequency f [see Fig. 4(a)]. Although we cannot directly control if the reduction of beating frequency is induced only by the reduction of oxygen or of other nutrients, sperms clearly reduce their activity and, as a consequence, their energy consumption. During the experiment we also observed a decay of both D and J [see Fig. 4(b)] and most importantly of the maximum precision p_{\max} by more than a order of magnitude [see Fig. 4(c)]. Remarkably, the observed decay of p_{\max} is well reproduced by the decay of energy consumption *normalized* by N , i.e., $p_{\max} \approx \dot{W}/(Nk_B T)$, where $N = 10^5$ is an estimate of the number of dynein motor domains in a flagellum [26–28] [see the blue solid and dashed lines in the inset of Fig. 4(c)]. We interpret this result as an argument in favor of the conjecture that fluctuations in the flagellum beating are dominated by fluctuations of spatially correlated dynein motors.

VII. GENERALIZATION TO OTHER EUKARYOTIC FLAGELLA: A TUR-BASED CORRELATION LENGTH

We underline that, in order to extrapolate it to other systems and more general conditions, the identification with N for the ratio between the TUR bound and the actual sperm precision should be taken as an order of magnitude. Here we discuss this point in detail. We propose to generalize our observation to assemblies of N molecular motors in the form

$p_{\max} \approx \dot{W}/\mathcal{L}_{\text{TUR}} k_B T$, where $\mathcal{L}_{\text{TUR}} \sim N$ is a correlation length (measured in adimensional units, i.e., as an estimate of the number of adjacent correlated motors). In Appendix B 3 we show that such a generalization follows by considering a chain of molecular motors whose dynamics is correlated up to an extension of approximately \mathcal{L}_{TUR} adjacent motors, leading to a renormalization of the precision by a factor \mathcal{L}_{TUR} . In order to corroborate our conjecture, we reconsidered several previous results where the quality factor for fluctuations was measured in different conditions and with different flagella (from sperms and *C. reinhardtii* algae) [16–20]. A summary of our and previous results is given in Table I, in Appendix B 4. Our conjecture allows us to collapse new and old data upon a master curve $\mathcal{L}_{\text{TUR}} \sim N$, fully consistent with our hypothesis (see Fig. 5).

VIII. CONCLUSIONS AND OUTLOOK

We have reported an experimental protocol to estimate the statistical precision of sperm's beating, which differs from previous measurements of the quality factor as it is directly related to energy consumption, according to the recently celebrated TURs. The use of single-cell traps aids the reconstruction of the dynamics of a single cell's shape, but in future implementations it could be replaced by a comoving tracking analysis directly applied upon free-swimming cells.

Our results point to the need of understanding dynamical fluctuations of active flagella and their relation to their bioenergetics [59–61]. It seems that a recognized theoretical statement, the thermodynamic uncertainty relation, has a relevance not only for molecular motors but also for mesoscopic self-propelling microswimmers. With this aim, we have reported two striking observations: (i) the coincidence between the maximum precision of the whole sperm cell and that of

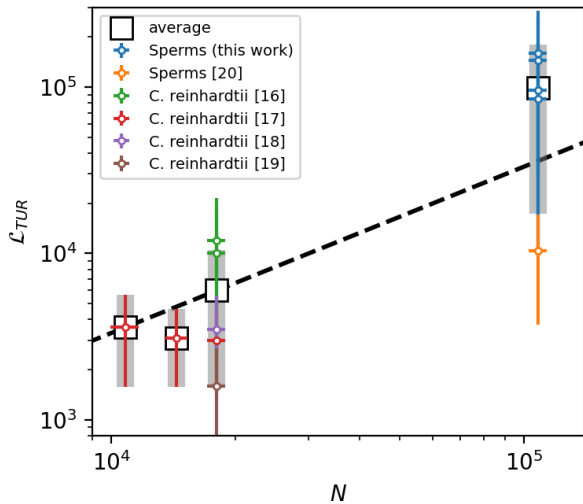


FIG. 5. Collapse of correlation lengths in several experiments. The data from different previous experiments with sperms and flagella of *C. reinhardtii* algae are summarized here by plotting the correlation length $\mathcal{L}_{\text{TUR}} = \frac{\dot{W}}{pk_B T}$, discussed in Appendix B 3, versus the length of the flagella N (both quantities are given as numbers of molecular motors). The data are also reported in Table I. The light colored points allow one to distinguish the different experiments, while the circles identify the averages at each given flagellar length. Bars represent statistical errors. The dashed line marks the scaling law $\mathcal{L}_{\text{TUR}} \sim N$, which is expected under the hypothesis of strong coordination among adjacent motors in the axoneme.

molecular motors actuating the sperm's flagellum and (ii) the dependence of the maximum precision of the whole sperm cell upon the reduction of energy consumption, a dependence that one would expect only for the molecular motors. As a common explanation we conjecture that the $N \approx 10^5$ dynein motors actuating a sperm's tail work at a high level of coordination which also affects fluctuations; a theoretical model where adjacent motors are coupled by a binding potential is consistent with our observations. The TUR is therefore still valid for the whole sperm's cell, but with a discrepancy between maximum precision and energy consumption which is approximately N times worse than in the case of the single molecular motor. An interesting perspective involves studying the same observables with other microswimmers, such as *E. coli*, whose flagellar motor fluctuations have been studied in the past [62] but not their connection with the TUR. It will also be important to understand more deeply the detailed mechanical modeling of ciliary oscillations and how fluctuations can emerge from the dynamical instabilities that underlie the axonemal beating [63–65]. Validating such models will require a comparison with the full probability density function of the beating phase fluctuations (and not only its extreme values).

We conclude by emphasizing that our work suggests new applications of the TUR and of the precision observable. First, the TUR lets us evaluate if the observed precision is low or not, as it gives a theoretical bound which can be reached by certain systems (for instance, some kinds of molecular motors get quite close to it). A large distance from such a bound is an observation which stimulates further investigation. Second, the precision p helped us in validating the theoretical model:

The scaling of p with N suggests the relevance of the coupling ingredient, beyond any precise calibration of the model parameters. Finally, p could be made useful, in the future, in fertility studies and diagnostics, as it can enter the list of parameters measured in a spermogram, to assess the health of human or animal sperm: For instance, our study suggests that it is correlated to the energy consumption of the cell. Of course, the usefulness of such a parameter (e.g., if it is correlated with the good performance of a cell in chemotaxis or other kinds of migration mechanisms) must be validated with further studies.

ACKNOWLEDGMENTS

A.P. and B.N. acknowledge financial support from Regione Lazio through the Grant “Progetti Gruppi di Ricerca” No. 85-2017-15257 and from the MIUR PRIN Project No. 201798CZLJ.

APPENDIX A: EXPERIMENT

1. Microfabrication

The microcage features allows us to accommodate one single cell on it, in a way that the head is confined while leaving the entire tail outside. Based on sperm characteristics, the chamber is designed as a box composed of four microfabricated facets anchored to the cover glass. The height, width, and depth of a single cage are 500 nm, 5.5 μm , and 11 μm , respectively. Microfabrication is carried out by a custom-built two-photon polymerization setup [66]. The microchambers are generated from SU-8 3025 photoresist (Kayaku Advanced Materials) using a 60×1.4 numerical aperture objective. After exposure, the photoresist sample is baked, ramping the temperature from 65 $^{\circ}\text{C}$ up to 95 $^{\circ}\text{C}$ with increments of 5 $^{\circ}\text{C}$ per min and then 7 min at the highest temperature. Reduction of stress between the substrate and SU-8 is achieved by gradually decreasing the temperature of the sample until reaching room temperature. Thereafter, the photoresist is developed by its standard developer solvent, followed by rinsing in a 1:1 solution of water and ethanol, and finally dried with a gentle blow of nitrogen. Strong adhesion of the microchambers to the carrier cover glass is ensured by three layers of Omnicoat adhesion promoter (Kayaku Advanced Materials). Laser power and scanning speed are 5 mW and 30 $\mu\text{m s}^{-1}$, respectively.

2. Sample preparation

The experiments for measuring the main spatial modes of the sperm's tail were developed on an open sample. This sample was obtained by attaching a plastic ring surrounding the microchambers area using the optical adhesive NOA81 (Norland Products Inc.). For the experiments under oxygen deprivation, we used hermetically sealed samples. Two fishing wires of approximately 100 μm thickness and NOA81 adhesive were used as spacers between the carrier cover glass and a coverslip, generating a channel; after introducing approximately 150 μL of solution containing sperm cells, the sample was completely sealed by applying NOA81 adhesive in the two open sides.

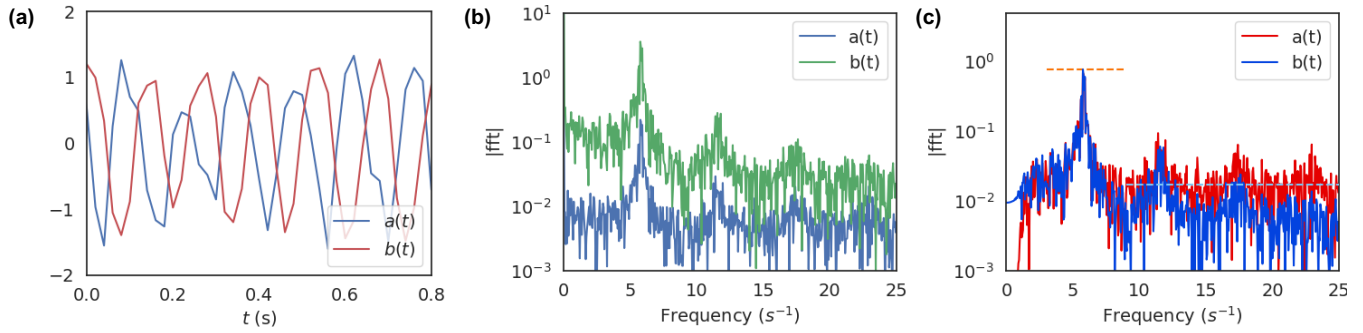


FIG. 6. Details about the tail-tracking procedure. (a) Examples of the signals $a(t)$ and $b(t)$ from trail tracking. One can see that $a(t)$ anticipates $b(t)$ of an angle between approximately $\pi/2$ and approximately π . (b) Spectra (modulus of the fast Fourier transform) of the signals $a(t)$ and $b(t)$. (c) Spectra after signal filtering. The orange and light blue dashed lines indicate the signal level and the noise level, respectively (the noise-to-signal ratio is defined as the ratio between the latter and the former).

Bull sperms were obtained from Agrilinea S.R.L. (Rome) and stored in a liquid nitrogen cylinder. On the day of the experiment, a vial of sperms suspended in semen was taken and immersed in a hot water bath of 37°C for 10 min. The vial was then taken out of the bath and immediately cut open using a pair of sterilized scissors. The sperm suspension was poured out of the vial in an Eppendorf. A micropipette was then used to suck out $150\ \mu\text{L}$ of the sperm suspension from the Eppendorf and insert the fluid into the microchannel, ensuring proper filling inside the structures. The sperm movement was recorded at environmental temperature, approximately 20°C , by using a digital camera (Nikon, USA) connected to an inverted microscope. The image capturing and analysis was performed using an in-house software made using PYTHON programming language

APPENDIX B: DATA ANALYSIS

1. Details about the tail-tracking procedure

Images are collected at 50 frames per second, with $20\times$ objective resulting in a resolution of $6.5/20\ \mu\text{m}$ per pixel. Each image portrays a large portion of the substrate where several cages are present, almost all filled by caged sperms. Only cages with a single trapped sperm cell are analyzed. A region of interest of on average 40×40 pixels, corresponding to an area of roughly $13 \times 13\ \mu\text{m}^2$, containing the most visible part of the tail which is also the one closest to the head [see Fig. 1(d)], is cropped and treated by successive layers of image processing tools: (i) background subtraction to reduce noise, (ii) transform to gradient (squared modulus) to avoid dependence on absolute levels, (iii) Gaussian filter with 1 pixel range, (iv) the largest continuous bright region is individuated (it always corresponds to the tail), and (v) that region is treated as a cloud of scattered points representing a curve y vs x , which is fitted by least squares to a second-order polynomial $y(x, t) = a(t) + b(t)x + c(t)x^2$ as discussed in the main text. The time series of $a(t)$ and $b(t)$ are filtered by a third-order Butterworth high-pass digital filter with critical frequency set at 1.5 Hz. In Fig. 6 the time series of $a(t)$ and $b(t)$ of a tracked cell are shown together with the spectra of the two series before and after the filtering. The noise-to-signal ratio is computed as the ratio between the noise level and the signal level, both shown in the figure.

2. Discussion of thermal diffusion effects due to the fluid

The value of D is the result of a complex interplay of elasticity, hydrodynamics, activity, and noises with different origins. Even at thermal equilibrium, i.e., for dead sperms, an estimate of filament phase diffusivity is complex as it involves not only the amplitude of fluctuations, which can be inferred by the equilibrium distribution of elastic energy, but also the relaxation time of such modes. A first estimate of involved timescales can be obtained by computing the rotational diffusivity. For a passive rod [67] (or a filament with low flexibility) of length $\ell \approx 50\ \mu\text{m}$ (as the sperm's body) in water viscosity η one has a rotational diffusivity of the order $D_{\text{Stokes}} \approx k_B T / \eta \ell^3 \approx 10^{-5}\ \text{rad}^2\ \text{s}^{-1}$. Visual inspection of our samples shows that nonmotile cells are basically immobile with negligible fluctuations in position or in shape, within our space-time resolution.

3. Correlation length based upon the thermodynamic uncertainty relation

Here we discuss a simple scaling argument to pinpoint the minimal assumptions behind the definition of an uncertainty correlation length

$$\mathcal{L}_{\text{TUR}} = \frac{\dot{W}}{p_N k_B T} \quad (\text{B1})$$

for a system of N connected motors (e.g., a chain similar to the axoneme structure). We recall that the asymptotic (steady-state) precision p is defined as

$$p_N = \lim_{t \rightarrow \infty} \frac{1}{t} \frac{\langle X_N(t) \rangle^2}{\langle X_N^2 \rangle_c}, \quad (\text{B2})$$

where $\langle x^2 \rangle_c$ stands for the variance of variable x and $X_N(t) = \int_0^t ds X_N(s)$ is the observed integrated current.

In a first-order approximation, the presence of spatial correlations across a correlation length \tilde{N} inside the chain can be accounted for by regrouping the N motors in $M = N/\tilde{N}$ independent groups. Moreover, the observed integrated current X_N can be assumed to be an empirical average of the integrated current in each of the M independent groups, i.e.,

$$X_N = \frac{\sum_{i=1}^M X_{N,i}}{M}, \quad (\text{B3})$$

TABLE I. Results from previous literature and from the present study for both sperms and *Chlamydomonas*. The columns report the kind of experiment (with reference), the frequency of beating (in hertz), the length of the flagellum (in microns), the estimated number of motors $N = 1800L$, the energy consumption in units of $k_B T$, the quality factor q (when measured), the maximum observed precision p_{\max} (in s^{-1}), and the precision-based correlation length $\mathcal{L}_{\text{TUR}} = \dot{W}/(pk_B T)$ in the number of motors (see Appendix B 3). To conserve space, we have not reported the errors if they can be computed by standard error propagation. The reported errors are those obtained from estimates reported in the literature and standard deviations in our experimental observations.

Experiment	f (Hz)	L (μm)	N	$\dot{W}/(k_B T)$	q	p_{\max} (s^{-1})	\mathcal{L}_{TUR}
Sperms (this study)	8 ± 1	60 ± 3	1.1×10^5	10^7		120 ± 30	8.5×10^4
Sperms after ~ 2 h	6 ± 1	60 ± 3	1.1×10^5	5.7×10^6		60 ± 10	9.6×10^4
Sperm after ~ 4 h	3 ± 1	60 ± 3	1.1×10^5	1.4×10^6		10 ± 5	1.4×10^5
Sperm after ~ 5 h	2 ± 1	60 ± 3	1.1×10^5	6.4×10^5		4 ± 0.5	1.6×10^5
Sperms at 37°C [20]	31 ± 1	60 ± 3	1.1×10^5	1.5×10^8	38 ± 5	1.4×10^4	10^4
<i>Chlamydomonas</i> [16]	47 ± 2	10 ± 0.5	1.8×10^4	1.6×10^8	23 ± 16	1.3×10^4	1.2×10^4
<i>Chlamydomonas</i> [16]	47 ± 2	10 ± 0.5	1.8×10^4	1.6×10^8	26 ± 18	1.6×10^4	10^4
<i>Chlamydomonas</i> [17]	71 ± 2	6 ± 0.5	10^4	2.3×10^8	70 ± 10	6.2×10^4	3.6×10^3
<i>Chlamydomonas</i> [17]	67 ± 2	8 ± 0.5	1.4×10^4	2.6×10^8	100 ± 12	8.3×10^4	3.1×10^3
<i>Chlamydomonas</i> [17]	62 ± 2	10 ± 0.5	1.8×10^4	2.9×10^8	120 ± 18	9.6×10^4	3×10^3
<i>Chlamydomonas</i> [18]	60 ± 3	10 ± 0.5	1.8×10^4	2.7×10^8	100 ± 20	7.5×10^4	3.5×10^3
<i>Chlamydomonas</i> [19]	53 ± 2	10 ± 0.5	1.8×10^4	2×10^8	199 ± 20	1.3×10^5	1.6×10^3

with the $X_{\tilde{N},i}$ being independent and identically distributed. These assumptions lead to

$$p_N = \lim_{t \rightarrow \infty} \frac{1}{t} \frac{\langle X_{\tilde{N}}(t) \rangle^2}{\langle X_{\tilde{N}}^2 \rangle / M} = M p_{\tilde{N}}. \quad (\text{B4})$$

Assuming that the mean consumed work is extensive in the size of the chain, i.e., $\dot{W}_N \sim N \dot{W}_1$, we get

$$\frac{\dot{W}_N}{p_N k_B T} = \tilde{N} \frac{\dot{W}_1}{p_{\tilde{N}}} = (Q_{\text{micro}})^{-1} \tilde{N}, \quad (\text{B5})$$

having considered

$$\frac{\dot{W}_1}{p_{\tilde{N}}} \approx \frac{\dot{W}_1}{p_1} = (Q_{\text{micro}})^{-1}. \quad (\text{B6})$$

In the last passage we have assumed $p_{\tilde{N}} \approx p_1$ following the assumption that for the correlated \tilde{N} motors in a group the precision is that of a single motor. Equation (B5) justifies our definition in Eq. (B1).

4. Previous experiments with sperms at physiological temperature and with other flagella

In a recent work [20] data from sperm cells observed at 37°C were analyzed. Such data, collected in a previous work [63], concern an anomalous swimming regime which is apparently induced by a particular sample preparation: They were ‘‘incubated with 1% F-127 (Sigma) in PBS for 5 min. ... When the surface was treated with F-127, the sperm did not stick but instead swam close to the surface, usually in circles of radii on the order of $40 \mu\text{m}$ ’’ [63]. With such treatment the measured beating frequency was particularly high; we define it as $f_{\text{Ma}} \sim 31$ Hz, much higher than what is usually observed (literature reports 20 Hz for bull sperm cells at 37°C [49], observed also in [63] without such surface treatment). Within such particular conditions the authors measured a quality factor which, in our notation, reads $q = J/2D \sim 38$, which would correspond to a precision $p = 2qJ$.

Other experimental works have addressed the properties of noise in the beating of axonemes, particularly with *Chlamydomonas* flagella [15–19]. In Refs. [16,17] the quality factor of beating was obtained indirectly from the rate of phase slips in pairs of synchronized flagella (as well as directly from the distribution of beating periods), getting estimates in a range $q = 25$ – 120 , with average beating frequency $f = 50$ Hz.

A summary of such previous observations and a comparison with the results of the present study are given in Table I. In compiling this table we have used some assumptions typically found in the literature i.e., that the amplitude of sperm’s beating is $6 \pm 1 \mu\text{m}$, the amplitude (‘‘wingspan’’) of *Chlamydomonas* flagellar beating is $10 \pm 1 \mu\text{m}$, and the energy consumption in both cases is given by the Taylor formula [Eq. (4)] multiplied by 10 (that is, assuming an average efficiency of 10%).

A plot of the TUR-based correlation length versus the length of the flagellum is shown in Fig. 5. Within the error, the data are compatible with long-range order, i.e., $\mathcal{L}_{\text{TUR}} \sim N$.

5. Estimates of the energy consumption and efficiency of sperm swimming

Consumption rate, speed, and beating frequency are sensitive to environmental conditions, e.g., temperature and fluid viscosity [49]. In Ref. [47] sea urchin sperm was studied in a 50% glycerol solution at 16°C with varying the beating frequencies through modulation of the ATP concentration: For instance, at 20 Hz, 10^6 molecules of ATP were found per sperm per second, corresponding to slightly more than approximately $10^7 k_B T$ per second. In Ref. [48] experiments were performed at 37°C , with bull semen diluted or washed in egg yolk with diluents, a phosphate buffer, and the addition of fructose and lactate, leading to an estimate of consumption rate equal to approximately 10^7 molecules of ATP per sperm per second, i.e., slightly more than approximately $10^8 k_B T$ per second. The evaluation of the produced work through the Taylor formula led to an estimate of the efficiency of

approximately 20%. In Ref. [27] sea urchin sperms were studied one by one in droplet solutions, at unreported temperature but with controlled conditions in both ATP concentration and buffer viscosity (both directly modulating the beating frequency), obtaining approximately 3×10^6 ATP molecules per sperm per second when the tail beats at 10 Hz.

APPENDIX C: A THEORETICAL MODEL FOR THE FLUCTUATIONS OF AN ACTIVE AXONEME

The model discussed in this Appendix is a variation of the classical model introduced in Ref. [12] and further studied in Refs. [57,58]. Interestingly, the original model has been used to rationalize recent experiments on sperm swimming fluctuations [20]. In the original model however, the fluctuations of the N motors are independent. Therefore, the fluctuations of the filament macroscopic dynamics are somehow similar to the fluctuations of an *average* of N independent noises and therefore their squared error (or diffusivity) decreases with N ; this results in a linear approximately N increase of the precision (or quality factor). We provide a simple mechanism to couple the noises of the motors and verify, in numerical simulations, that this ingredient is sufficient, at strong coupling, to change the size scaling from $O(N)$ to $O(1)$.

In the model the filament is represented by a position $X(t)$ and by a potential $W = \sum_{i=1}^N s_i U[x_i - X(t)]$ which regulates the interaction of the filament with N motors, each one being at fixed position x_i and in attachment state $s_i = 0, 1$ (0 when detached and 1 when attached). The position $X(t)$ can be understood as the real position in space of the center of mass of the filament, as well as a generalized coordinate representing the shape of it. The potential may be related to local properties of the filament, such as the local curvature which depends upon the time t through the coordinate $X(t)$. Each motor can detach from and reattach to the filament, changing its state s_i , according to a Poisson process that violates detailed balance, as it happens when the $\text{ATP} \rightarrow \text{ADP} + \text{P}$ process is involved. The overdamped equation of motion of the filament is $\xi \dot{X}(t) = F_{\text{ext}}(t) + F(t)$, where $F(t) = -\partial_X \sum_i s_i U[x_i - X(t)]$ and $F_{\text{ext}}(t)$ is an external force. In general, the filament can be free from external forces, but then a spatial asymmetry [employed in $W(x)$] is needed to induce forward motion; otherwise an external force (e.g., a spring on an end of the filament) is already sufficient to break spatial symmetry and the potential W can be taken to be symmetric to simplify calculations. This is the case analyzed here and in Ref. [20], with $F_{\text{ext}} = -\kappa X$ and $U(x) = U_0[1 - \cos(2\pi x/\ell)]$, the filament does not move on average but fluctuates more or less regularly, while a limit cycle in the $X(t)$ - $F(t)$ plane can be used as analogous to the A - B plane used in our experiments. In the original model, each motor realizes the attachment-detachment process independently of the other motors, with the only indirect correlations due to the modulation of the attachment-detachment rate through the position $\omega_{\text{on}}^i = \Omega(\eta - \alpha \cos\{2\pi[x_i - X(t)]/\ell\})$ and $\omega_{\text{off}}^i = \Omega - \omega_{\text{on}}^i$. This ingredient, however, only correlates (locally) the average residence times but does not correlate fluctuations around those averages: It is the same as considering independent noises with similar averages.

In order to adapt the model to our experimental findings, we introduced a binding potential that correlates adjacent motors: This potential is minimized when adjacent motors are in the same state. This is implemented as a modification of the rates according to the formula $\omega_{\text{on}}^i = \Omega(\eta - \alpha \cos\{2\pi[x_i - X(t)]/\ell\})e^{-\Delta U_i^{\text{bind}}}$ and $\omega_{\text{off}}^i = \Omega - \Omega(\eta - \alpha \cos\{2\pi[x_i - X(t)]/\ell\})e^{-\Delta U_i^{\text{bind}}}$, where ΔU_i^{bind} is the binding potential increase after the variation of state s_i of the i th motor and the binding potential is $U_i^{\text{bind}} = K(s_i - s_{i+1})^2 + K(s_i - s_{i-1})^2$. When $K = 0$ the original model without binding energy is recovered.

The effect of K can be appreciated in numerical simulations of the model whose results are reported in Figs. 3 and 7. In particular, in Figs. 7(c)–7(f) we show the drastic change in the decay of the phase correlation when K is increased. In Fig. 3(b) it can be appreciated how the size scaling of the precision changes completely and tends to become *independent* of N when the coupling strength increases. Our observation that the macroscopic sperm precision ($N \sim 10^5$) is similar to the microscopic sperm precision ($N = 1$) is explained fairly well by this new model. Note that the beating frequency in the model is independent of N (at least for $N \gtrsim 10^2$) so that the energy consumption (ATP consumed per cycle and per motor) increases with N , even for large binding potential. The ratio between precision $p \sim O(1)$ and energy consumption $\dot{W} \sim N$ is therefore doomed to decrease as $1/N$, in fair agreement with experimental observations.

APPENDIX D: SIMPLEST WORKING PRINCIPLE FOR THERMODYNAMIC UNCERTAINTY RELATIONS

While the TURs have been demonstrated for larger and larger classes of models and time domains, we judge it instructive to summarize the first example where they have been observed, which is a Markov jump process describing, in a very simplified way, the stochastic (progressive on average) dynamics of a single Brownian motor or clock [23]. The model is defined in continuous time; the motor can go forward or backward with probability rates k_+ and k_- , respectively. Local detailed balance dictates that $k_+/k_- \sim \exp(Q/k_B T)$, where $Q = W$ is the energy dissipated in a forward jump equal to the work input carried by ATP.

The average current of the clock (number of steps per unit of time) is $J = k_+ - k_-$, while the associated diffusivity is $2D = k_+ + k_-$. Therefore, for the position $X(t)$ of the motor or clock one has a relative uncertainty defined as $\epsilon^2 = (\langle X^2 \rangle - \langle X \rangle^2)/\langle X \rangle^2$, which reads $\epsilon^2 = 2Dt/(Jt)^2 = (k_+ + k_-)/(k_+ - k_-)^2 t$, which in terms of the precision $p = 2/t\epsilon^2$ reads $p = 2(k_+ - k_-)^2/(k_+ + k_-)$. The energy dissipated up to time t reads, in terms of the entropy production rate σ , $T\sigma t = \dot{Q}t = JQ t$. Then the product between the energy dissipated and the relative uncertainty satisfies $2\dot{Q}/p = T\sigma t\epsilon^2 = (k_+ + k_-)/(k_+ - k_-)Q \coth(Q/2k_B T) \geq 2k_B T$, which leads to the TUR used in this paper $p \leq \dot{Q}/k_B T$.

This example is useful to evaluate the key sources of noise in this process, i.e., the contributions to D which are both k_+ and k_- . This means that backstepping (a non-negligible k_-) is not the only source of noise, but k_+ also contributes to noise. The reason is that a large contribution to fluctuations of the motor current is due to fluctuations in the residence

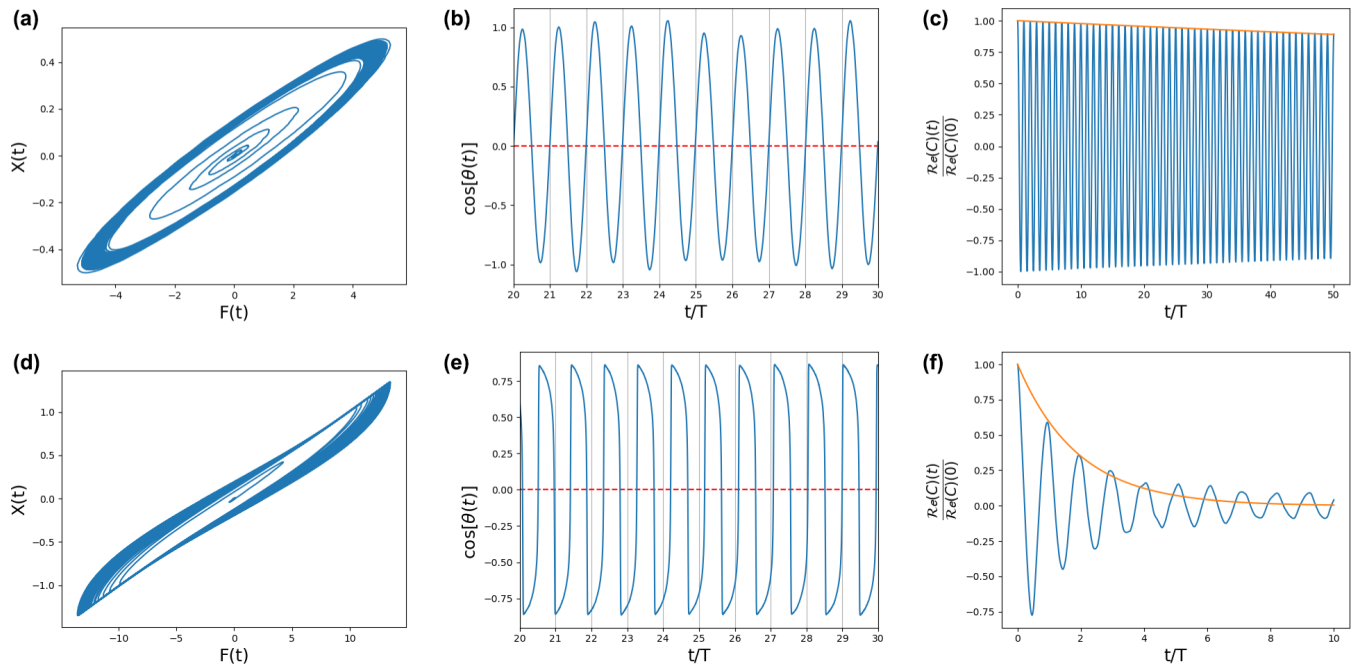


FIG. 7. Theoretical model. (a) and (d) Evolution of the system in the force-coordinate phase space: (a) $K = 0$ and (d) $K = 10$. The angle $\theta(t)$ measures the phase of this limit cycle after suitable rotation and normalization of the axis. (b) and (e) Evolution of $\cos[\theta(t)]$ that allows us to evaluate the stability of the periods in the two cases: (b) $K = 0$ and (e) $K = 10$. (c) and (f) Real part of the autocorrelation of $e^{i\theta(t)}$ and exponential fit of approximately $e^{-\lambda t}$ of its envelope: (c) $K = 0$ and (f) $K = 10$. In all the simulations we have used $\alpha = \eta = 0.5$, $k/\xi\Omega = 10$, and $\alpha NU_0/\Omega\ell^2\xi = 0.6$.

time before a new forward step. If time is discretized in dt steps, the motor remains in its position with a probability $1 - (k_+)dt - (k_-)dt$; the exit time has an exponential probability with average exit rate $(k_+) + (k_-)$. The real chemical network of a molecular motor, such as the dynein, is much richer than the minimal model considered in Refs. [23,68,69]. In that minimal model a single step is a coarse graining of the several intermediate chemical steps. The presence of intermediate

steps with their fluctuating residence of times and possibly non-negligible backstepping probabilities implies relevant fluctuations in the coarse-grained residence times and therefore in the motor's current, even when the total backstepping probability is negligible. We deem these motors' fluctuations, with an additional coordination hypothesis discussed in the text, to be important for the deviation of the sperm shape cycle from its average dynamics.

- [1] E. Lauga and T. R. Powers, The hydrodynamics of swimming microorganisms, *Rep. Prog. Phys.* **72**, 096601 (2009).
- [2] J. Elgeti, R. G. Winkler, and G. Gompper, Physics of microswimmers—single particle motion and collective behavior: A review, *Rep. Prog. Phys.* **78**, 056601 (2015).
- [3] L. J. Fauci and R. Dillon, Biofluidmechanics of reproduction, *Annu. Rev. Fluid Mech.* **38**, 371 (2006).
- [4] A. C. H. Tsang, E. Demir, Y. Ding, and O. S. Pak, Roads to smart artificial microswimmers, *Adv. Intel. Syst.* **2**, 1900137 (2020).
- [5] C. B. Lindemann and K. A. Lesich, Functional anatomy of the mammalian sperm flagellum, *Cytoskeleton* **73**, 652 (2016).
- [6] K. E. Machin, Wave propagation along flagella, *J. Exp. Biol.* **35**, 796 (1958).
- [7] J. Elgeti, U. B. Kaupp, and G. Gompper, Hydrodynamics of sperm cells near surfaces, *Biophys. J.* **99**, 1018 (2010).
- [8] E. A. Gaffney, H. Gad elha, D. J. Smith, J. R. Blake, and J. C. Kirkman-Brown, Mammalian sperm motility: Observation and theory, *Annu. Rev. Fluid Mech.* **43**, 501 (2011).
- [9] H. C. Crenshaw, Kinematics of helical motion of microorganisms capable of motion with four degrees of freedom, *Biophys. J.* **56**, 1029 (1989).
- [10] J. Gray and G. J. Hancock, The propulsion of sea-urchin spermatozoa, *J. Exp. Biol.* **32**, 802 (1955).
- [11] E. M. Purcell, Life at low Reynolds number, *Am. J. Phys.* **45**, 3 (1977).
- [12] F. J ulicher and J. Prost, Spontaneous Oscillations of Collective Molecular Motors, *Phys. Rev. Lett.* **78**, 4510 (1997).
- [13] B. M. Friedrich and F. J ulicher, The stochastic dance of circling sperm cells: Sperm chemotaxis in the plane, *New J. Phys.* **10**, 123025 (2008).
- [14] B. M. Friedrich and F. J ulicher, Steering Chiral Swimmers along Noisy Helical Paths, *Phys. Rev. Lett.* **103**, 068102 (2009).
- [15] M. Polin, I. Tuval, K. Drescher, J. P. Gollub, and R. E. Goldstein, *Chlamydomonas* swims with two “gears” in a eukaryotic version of run-and-tumble locomotion, *Science* **325**, 487 (2009).

- [16] R. E. Goldstein, M. Polin, and I. Tuval, Noise and Synchronization in Pairs of Beating Eukaryotic Flagella, *Phys. Rev. Lett.* **103**, 168103 (2009).
- [17] R. E. Goldstein, M. Polin, and I. Tuval, Emergence of Synchronized Beating during the Regrowth of Eukaryotic Flagella, *Phys. Rev. Lett.* **107**, 148103 (2011).
- [18] K. Y. Wan and R. E. Goldstein, Rhythmicity, Recurrence, and Recovery of Flagellar Beating, *Phys. Rev. Lett.* **113**, 238103 (2014).
- [19] G. Quaranta, M.-E. Aubin-Tam, and D. Tam, Hydrodynamics Versus Intracellular Coupling in the Synchronization of Eukaryotic Flagella, *Phys. Rev. Lett.* **115**, 238101 (2015).
- [20] R. Ma, G. S. Klindt, I. H. Riedel-Kruse, F. Jülicher, and B. M. Friedrich, Active Phase and Amplitude Fluctuations of Flagellar Beating, *Phys. Rev. Lett.* **113**, 048101 (2014).
- [21] G. S. Klindt and B. M. Friedrich, Flagellar swimmers oscillate between pusher- and puller-type swimming, *Phys. Rev. E* **92**, 063019 (2015).
- [22] A. Solovov and B. M. Friedrich, Synchronization in cilia carpets and the kuramoto model with local coupling: breakup of global synchronization in the presence of noise, *Chaos* **32**, 013124 (2022).
- [23] A. C. Barato and U. Seifert, Thermodynamic Uncertainty Relation for Biomolecular Processes, *Phys. Rev. Lett.* **114**, 158101 (2015).
- [24] T. R. Gingrich, J. M. Horowitz, N. Perunov, and J. L. England, Dissipation Bounds All Steady-State Current Fluctuations, *Phys. Rev. Lett.* **116**, 120601 (2016).
- [25] J. M. Horowitz and T. R. Gingrich, Thermodynamic uncertainty relations constrain non-equilibrium fluctuations, *Nat. Phys.* **16**, 15 (2020).
- [26] C. B. Lindemann, Structural-functional relationships of the dynein, spokes, and central-pair projections predicted from an analysis of the forces acting within a flagellum, *Biophys. J.* **84**, 4115 (2003).
- [27] D. T. N. Chen, M. Heymann, S. Fraden, D. Nicastro, and Z. Dogic, ATP consumption of eukaryotic flagella measured at a single-cell level, *Biophys. J.* **109**, 2562 (2015).
- [28] W. Gilpin, M. S. Bull, and M. Prakash, The multiscale physics of cilia and flagella, *Nat. Rev. Phys.* **2**, 74 (2020).
- [29] C. Bustamante, D. Keller, and G. Oster, The physics of molecular motors, *Acc. Chem. Res.* **34**, 412 (2001).
- [30] C. J. Brokaw, Thinking about flagellar oscillation, *Cell Motil. Cytoskel.* **66**, 425 (2009).
- [31] C. J. Brokaw, Computer simulation of flagellar movement VIII: Coordination of dynein by local curvature control can generate helical bending waves, *Cell Motil. Cytoskel.* **53**, 103 (2002).
- [32] S. A. Burgess, Rigor and relaxed outer dynein arms in replicas of cryofixed motile flagella, *J. Mol. Biol.* **250**, 52 (1995).
- [33] U. W. Goodenough and J. E. Heuser, Substructure of the outer dynein arm, *J. Cell Biol.* **95**, 798 (1982).
- [34] W. Hwang and C. Hyeon, Energetic costs, precision, and transport efficiency of molecular motors, *J. Phys. Chem. Lett.* **9**, 513 (2018).
- [35] G. Falasco and M. Esposito, Dissipation-Time Uncertainty Relation, *Phys. Rev. Lett.* **125**, 120604 (2020).
- [36] R. Rikmenspoel, G. van Herpen, and P. Eijkhout, Cinematographic observations of the movements of bull sperm cells, *Phys. Med. Biol.* **5**, 167 (1960).
- [37] D. M. Woolley, Motility of spermatozoa at surfaces, *Reproduction* **126**, 259 (2003).
- [38] R. Nosrati, A. Driouchi, C. M. Yip, and D. Sinton, Two-dimensional slither swimming of sperm within a micrometre of a surface, *Nat. Commun.* **6**, 8703 (2015).
- [39] G. Saggiorato, L. Alvarez, J. F. Jikeli, U. B. Kaupp, G. Gompper, and J. Elgeti, Human sperm steer with second harmonics of the flagellar beat, *Nat. Commun.* **8**, 1415 (2017).
- [40] See Supplemental Material at <http://link.aps.org/supplemental/10.1103/PRXLife.1.013003> for the results of head oscillation tracking, a discussion of alternative estimates of the precision, a table of symbols used in the paper, and a video with a caged sperm cell, its tail digitally tracked, recorded at six different time delays with respect to the starting time of the oxygen deprivation experiment.
- [41] C. Battle, C. P. Broedersz, N. Fakhri, V. F. Geyer, J. Howard, C. F. Schmidt, and F. C. MacKintosh, Broken detailed balance at mesoscopic scales in active biological systems, *Science* **352**, 604 (2016).
- [42] J. Gladrow, C. P. Broedersz, and C. F. Schmidt, Nonequilibrium dynamics of probe filaments in actin-myosin networks, *Phys. Rev. E* **96**, 022408 (2017).
- [43] G. J. Stephens, B. Johnson-Kerner, W. Bialek, and W. S. Ryu, Dimensionality and dynamics in the behavior of *C. elegans*, *PLoS Comput. Biol.* **4**, e1000028 (2008).
- [44] F. S. Gnesotto, F. Mura, J. Gladrow, and C. P. Broedersz, Broken detailed balance and non-equilibrium dynamics in living systems: A review, *Rep. Prog. Phys.* **81**, 066601 (2018).
- [45] J. Li, J. M. Horowitz, T. R. Gingrich, and N. Fakhri, Quantifying dissipation using fluctuating currents, *Nat. Commun.* **10**, 1 (2019).
- [46] É. Roldán, J. Barral, P. Martin, J. M. R. Parrondo, and F. Jülicher, Quantifying entropy production in active fluctuations of the hair-cell bundle from time irreversibility and uncertainty relations, *New J. Phys.* **23**, 083013 (2021).
- [47] C. J. Brokaw, Adenosine triphosphate usage by flagella, *Science* **156**, 76 (1967).
- [48] R. Rikmenspoel, S. Sinton, and J. J. Janick, Energy conversion in bull sperm flagella, *J. Gen. Physiol.* **54**, 782 (1969).
- [49] R. Rikmenspoel, Movements and active moments of bull sperm flagella as a function of temperature and viscosity, *J. Exp. Biol.* **108**, 205 (1984).
- [50] C. J. Brokaw, Effects of increased viscosity on the movements of some invertebrate spermatozoa, *J. Exp. Biol.* **45**, 113 (1966).
- [51] C. J. Brokaw, Effects of viscosity and ATP concentration on the movement of reactivated sea-urchin sperm flagella, *J. Exp. Biol.* **62**, 701 (1975).
- [52] D. Nicastro, C. Schwartz, J. Pierson, R. Gaudette, M. E. Porter, and J. R. McIntosh, The molecular architecture of axonemes revealed by cryoelectron tomography, *Science* **313**, 944 (2006).
- [53] Z. Carvalho-Santos, J. Azimzadeh, J. B. Pereira-Leal, and M. Bettencourt-Dias, Evolution: Tracing the origins of centrioles, cilia, and flagella, *J. Cell Biol.* **194**, 165 (2011).
- [54] G. S. Klindt, C. Ruloff, C. Wagner, and B. M. Friedrich, Load Response of the Flagellar Beat, *Phys. Rev. Lett.* **117**, 258101 (2016).
- [55] N. Pellicciotta, E. Hamilton, J. Kotar, M. Faucourt, N. Delgehr, N. Spassky, and P. Cicuta, Entrainment of mammalian motile cilia in the brain with hydrodynamic forces, *Proc. Natl. Acad. Sci. USA* **117**, 8315 (2020).

- [56] We remark that in Ref. [34] cytoplasmic dynein is considered, which is known to be structurally similar to the axonemal one, with also a few distinct features [70].
- [57] T. Guérin, J. Prost, and J.-F. Joanny, Dynamical behavior of molecular motor assemblies in the rigid and crossbridge models, *Eur. Phys. J. E* **34**, 1 (2011).
- [58] T. Guérin, J. Prost, and J.-F. Joanny, Bidirectional motion of motor assemblies and the weak-noise escape problem, *Phys. Rev. E* **84**, 041901 (2011).
- [59] D. J. Skinner and J. Dunkel, Improved bounds on entropy production in living systems, *Proc. Natl. Acad. Sci. USA* **118**, e2024300118 (2021).
- [60] X. Yang, M. Heinemann, J. Howard, G. Huber, S. Iyer-Biswas, G. Le Treut, M. Lynch, K. L. Montooth, D. J. Needleman, S. Pigolotti *et al.*, Physical bioenergetics: Energy fluxes, budgets, and constraints in cells, *Proc. Natl. Acad. Sci. USA* **118**, e2026786118 (2021).
- [61] T. H. Tan, G. A. Watson, Y.-C. Chao, J. Li, T. R. Gingrich, J. M. Horowitz, and N. Fakhri, Scale-dependent irreversibility in living matter, [arXiv:2107.05701](https://arxiv.org/abs/2107.05701).
- [62] A. D. Samuel and H. C. Berg, Fluctuation analysis of rotational speeds of the bacterial flagellar motor, *Proc. Natl. Acad. Sci. USA* **92**, 3502 (1995).
- [63] I. H. Riedel-Kruse, A. Hilfinger, J. Howard, and F. Jülicher, How molecular motors shape the flagellar beat, *HFSP J.* **1**, 192 (2007).
- [64] P. Sartori, V. F. Geyer, A. Scholich, F. Jülicher, and J. Howard, Dynamic curvature regulation accounts for the symmetric and asymmetric beats of chlamydomonas flagella, *eLife* **5**, e13258 (2016).
- [65] D. Mondal, R. Adhikari, and P. Sharma, Internal friction controls active ciliary oscillations near the instability threshold, *Sci. Adv.* **6**, eabb0503 (2020).
- [66] G. Vizsnyiczai, G. Frangipane, C. Maggi, F. Saglimbeni, S. Bianchi, and R. Di Leonardo, Light controlled 3D micromotors powered by bacteria, *Nat. Commun.* **8**, 15974 (2017).
- [67] J. Elgeti and G. Gompper, Self-propelled rods near surfaces, *Europhys. Lett.* **85**, 38002 (2009).
- [68] J. Howard, *Mechanics of Motor Proteins and the Cytoskeleton* (Sinauer, Sunderland, 2001).
- [69] L. Peliti and S. Pigolotti, *Stochastic Thermodynamics: An Introduction* (Princeton University Press, Princeton, 2021).
- [70] Y. S. Kato, T. Yagi, S. A. Harris, S.-y. Ohki, K. Yura, Y. Shimizu, S. Honda, R. Kamiya, S. A. Burgess, and M. Tanokura, Structure of the microtubule-binding domain of flagellar dynein, *Structure* **22**, 1628 (2014).